

Multidimensional modelling of X-ray spectra for AGN accretion disc outflows

S. A. Sim,¹^{*} K. S. Long,² L. Miller³ and T. J. Turner^{4,5}

¹Max-Planck-Institut für Astrophysik, Karl-Schwarzschildstr. 1, 85748 Garching, Germany

²Space Telescope Science Institute, 3700 San Martin Drive, Baltimore, MD 21218, USA

³Department of Physics, University of Oxford, Denys Wilkinson Building, Keble Road, Oxford OX1 3RH

⁴Department of Physics, University of Maryland Baltimore County, 1000 Hilltop Circle, Baltimore, MD 21250, USA

⁵Astrophysics Science Division, NASA/GSFC, Greenbelt, MD 20771, USA

Accepted 2008 May 13. Received 2008 May 2; in original form 2008 April 5

ABSTRACT

We use a multidimensional Monte Carlo code to compute X-ray spectra for a variety of active galactic nucleus (AGN) disc–wind outflow geometries. We focus on the formation of blueshifted absorption features in the Fe K band and show that line features similar to those which have been reported in observations are often produced for lines of sight through disc–wind geometries. We also discuss the formation of other spectral features in highly ionized outflows. In particular, we show that, for sufficiently high wind densities, moderately strong Fe K emission lines can form and that electron scattering in the flow may cause these lines to develop extended red wings. We illustrate the potential relevance of such models to the interpretation of real X-ray data by comparison with observations of a well-known AGN, Mrk 766.

Key words: radiative transfer – methods: numerical – galaxies: active – X-rays: galaxies.

1 INTRODUCTION

The study of active galactic nuclei (AGN) is an important topic in contemporary astrophysics. These objects are interesting in their own right, allowing us to study the extreme physics of accretion in the vicinity of a supermassive black hole. Furthermore, numerical simulations suggest that AGN likely have a critical role in the formation and evolution of galaxies, highlighting the need to understand how these objects accrete matter, grow and feedback energy to their surroundings (e.g. Croton et al. 2006).

Since AGN are bright X-ray sources, they have been popular targets for almost all X-ray observatories. One of the most interesting results obtained thanks to the high sensitivity of the current generation of X-ray missions [specifically *XMM-Newton* (Jansen et al. 2001), *Chandra* (Weisskopf et al. 2002) and, more recently, *Suzaku* (Mitsuda et al. 2007)] has been the detection of narrow absorption features in the 2–10 keV band of several bright AGN (see e.g. Pounds et al. 2003a; Reeves et al. 2004; Risaliti et al. 2005; Young et al. 2005; Baito et al. 2007; Turner et al. 2007). Particularly for features in the Fe K region of the spectrum, the observed energies and strengths of these lines suggest identification with very highly ionized species (e.g. Fe xxv and Fe xxvi) in very fast (up to $\sim 0.1c$) outflows. Blueshifted absorption lines are well known from observations of AGN in other wavebands and models explaining

such phenomena in terms of winds have been developed (see e.g. Murray et al. 1995; Elvis 2000; Proga & Kallman 2004). However, the new X-ray data clearly suggest a component of very highly ionized fast outflowing plasma, the relationship of which to the less ionized material observable in ultraviolet (UV) or softer X-ray wavebands remains unclear. In particular, moderately ionized outflows identified in soft X-ray spectra generally have somewhat lower velocity ($\lesssim 1000 \text{ km s}^{-1}$; Blustin et al. 2005; McKernan, Yaqoob & Reynolds 2007) while UV spectra can show evidence of either low or high velocity absorption (e.g. Elvis 2000).

As observational evidence in support of the phenomenon has accumulated, several theoretical studies of the physical properties of highly ionized AGN outflows have been made. Pounds et al. (2003a) and King & Pounds (2003) discussed the blueshifted absorption features in PG1211+143 in terms of a conical outflow subtending a large solid angle. They suggested that such a flow might be driven by continuum radiation pressure and that emission from such a flow might be responsible for the big blue bump which dominates the bolometric output of PG1211+143. However, Everett & Ballantyne (2004) considered flows driven by continuum radiation pressure in greater detail and concluded that, while this mechanism could work in principle, the resulting outflows were unlikely to produce spectral signatures as strong as those reported by Pounds et al. (2003a).

Sim (2005) undertook a 2D Monte Carlo (MC) radiative transfer study of parametrized conical outflow models and concluded that, for suitable column densities, viewing down such flows could account for the observed blueshifted, narrow absorption lines in

*E-mail: ssim@mpa-garching.mpg.de

PG1211+143. However, that study was limited to consideration of only the simplest conical geometry and did not consider the effect of either rotation or off-axis lines of sight on the spectrum.

Using a chained version of the 1D *XSTAR* code (Kallman & Bautista 2001), Schurch & Done (2007, 2008) have computed spectra for columns of outflowing gas with a variety of density and velocity profiles. They demonstrated that outflows can imprint a wide variety of features on X-ray spectra, depending on the outflow conditions and that very high outflow velocities would be required if absorption in outflows is to explain soft excesses in AGN spectra. More recently, a similar approach to that adopted by Schurch & Done (2007) has been used for the calculation of transmission spectra in dynamical models of AGN outflows by Dorodnitsyn, Kallman & Proga (2008).

In this paper, we extend the study of Sim (2005) to incorporate a more realistic and more versatile description of a disc wind geometry including both rotation and off-axis lines of sight. We retain the use of the MC method owing to its versatility for multidimensional radiative transfer. Our method is complementary to that of Schurch & Done (2007) since we account for geometric effects directly (e.g. scattering of radiation between lines of sight in multidimensional outflow geometries) but make some simplifications in the treatment of atomic processes.

We focus on highly ionized winds and the interpretation of observable features in the Fe K band. Although other spectral lines are expected to form in outflows, Fe K α absorption is the most relevant for the interpretation of observed spectra since it is the clearest signature of a highly ionized flow: although more abundant, the lighter elements are fully ionized more easily than Fe so that any spectral features they imprint are weaker. Furthermore, identification of features in the Fe K energy band is relatively secure since only K shell transitions of heavy ions are expected at energies $\gtrsim 5$ keV. At lower energies, where K α transitions of light or intermediate-mass elements might arise, line identification is more ambiguous, particularly if large velocity shifts are considered.

Although we regard Fe K α absorption features as the best diagnostic for a highly ionized flow, we will also investigate the formation of emission components in the Fe K region arising from line scattering or recombination in the outflow. Such features are of particular interest since they may explain possible P-Cygni-like line profiles (e.g. Done et al. 2007; Turner et al. 2008) and may affect the interpretation of Fe emission features commonly associated with disc reflection (see e.g. Laming & Titarchuk 2004; Laurent & Titarchuk 2007).

We begin in Section 2 by defining the class of outflow models which we will consider. In Section 3 we describe our radiative transfer method and discuss the adopted atomic data. We present a sample calculation for one model in Section 4 and then extend our discussion to a grid of outflow models in Section 5. The implications of our models for observations of Fe K α absorption are described in Section 6 and for other spectral features in Section 7. In Section 8 we illustrate the value of our models by comparing them in detail with observations of a well-known AGN, Mrk 766. We draw conclusions and discuss further work in Section 9.

2 MODEL

Our radiative transfer calculations were performed using a simply parametrized model for an outflow launched from an accretion disc around a supermassive black hole. In this section, we describe the properties of the model and the parameters which must be specified to define a particular realization of the model.

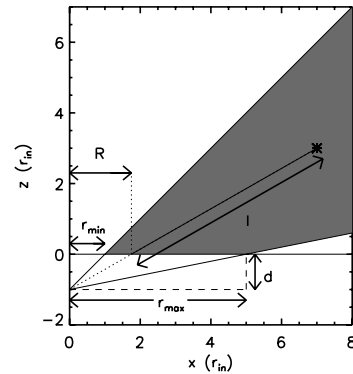


Figure 1. The geometrical construction used to define the wind (only the positive xz plane is shown – the wind is symmetric under both reflection in the xy plane and rotation about the z -axis). The region occupied by the wind is shaded. The three parameters which determine the geometry (d, r_{\min}, r_{\max}) are indicated. The star symbol represents the point in the wind which is specified by the wind coordinates R and l .

2.1 Geometry

We adopt a standard disc wind geometry, namely the ‘displaced dipole’ model of Knigge, Woods & Drew (1995). This geometry has been adopted in radiative transfer studies of accretion disc winds for a variety of systems including cataclysmic variables (Knigge et al. 1995; Long & Knigge 2002) and massive young stellar objects (Sim et al. 2005). The geometry is illustrated in Fig. 1 and is defined by the following three parameters (each of which is marked in the figure):

- (i) d , the distance of the focus point below the origin;
- (ii) r_{\min} , the distance from the origin to the inner edge of the wind in the xy plane;
- (iii) r_{\max} , the distance from the origin to the outer edge of the wind in the xy plane.

The accretion disc is assumed to lie in the xy plane. The wind is symmetric under rotation about the z -axis and under reflection in the xy plane.

2.2 Velocity law in the wind

The velocity is specified at every point in the wind following the parametrization of Knigge et al. (1995) (see also Long & Knigge 2002). Although this velocity law is not based on self-consistent hydrodynamical outflow models (cf. Dorodnitsyn et al. 2008), it provides a simple and reasonably flexible description of possible steady-state flows which we use for our exploratory radiative transfer simulations.

2.2.1 Rotation

The wind rotates about the z -axis. The rotational velocity is obtained by assuming that parcels of matter conserve specific angular momentum about the z -axis as they flow outwards. The angular momentum at the base of a streamline is set at the Keplerian value for the radius at which the streamline crosses the xy plane. Thus the rotational velocity is determined only by the choice of wind geometry (see above) and the mass of the central object, M_{bh} .

2.2.2 Outflow

The outflow velocity points directly away from the focus point of the wind. Its magnitude is given by

$$v_l = v_0 + (v_\infty - v_0) \left(1 - \frac{R_v}{R_v + l} \right)^\beta, \quad (1)$$

where l is the distance along the outflow streamline (see Fig. 1), R_v is an acceleration length parameter and the exponent, β , sets the rate of acceleration. The terminal velocity, v_∞ , is specified as a multiple f_v of the escape speed from the base of the streamline

$$v_\infty = f_v \sqrt{\frac{2GM_{\text{bh}}}{R}}, \quad (2)$$

where R is the radius at the base of the streamline (see Fig. 1).

2.3 Mass density

The wind is assumed to be smooth and in a steady-state flow; extension of this study to clumpy flows will be the topic of a subsequent investigation. The total mass-loss rate (\dot{M}) of the wind is treated as a parameter and the mass loading of specific outflow streamlines is determined by parametrizing the mass-loss rate per unit surface area as a function of R via

$$\frac{d\dot{m}}{dA} \propto R^k, \quad (3)$$

subject to the constraint that

$$4\pi \int_{r_{\min}}^{r_{\max}} \frac{d\dot{m}}{dA} R \, dR = \dot{M}. \quad (4)$$

The mass density at a point in the wind is then obtained by combining the specific mass-loss rate on local outflow streamlines with the outflow velocity, assuming a stationary flow.

2.4 Electron temperature

The electron temperature T_e of the outflowing material must be specified since it has a role to play in determining the ionization/excitation state of the plasma (see below). Ultimately, it should be calculated by consideration of all relevant heating and cooling processes. But the treatment of all such processes – heating and cooling via lines, bound–free continua, free–free processes and (inverse) Compton scattering of photons at all energies – would require more detailed atomic physics, simulations of a much wider range of photon energies and the self-consistent consideration of heating by radiation from other sources (e.g. radiation emitted or reflected by the accretion disc or surrounding structures). Such issues go beyond the scope of this study and so, as in Sim (2005), T_e is assumed to be uniform and is treated as an input parameter.

2.5 Atomic level populations

In order to keep the computational requirements of our multidimensional MC calculations tractable, we have not attempted a complete non-local thermodynamic equilibrium (non-LTE) calculation, but have instead employed approximate formulae for ionization and excitation. Our approach is similar to the standard modified nebular approximation, which has been used in a variety of other astrophysical calculations [e.g. stellar winds (Abbott & Lucy 1985; Lucy & Abbott 1993; Vink, de Koter & Lamers 1999), supernovae (Mazzali & Lucy 1993) and disc winds from cataclysmic variables (Long &

Knigge 2002)]. However, as discussed in Section 3.4, we have modified standard approximations to reflect the fact that X-ray spectra of AGN are better approximated by a power law than a blackbody.

2.5.1 Ionization

For simplicity, we assume ionization equilibrium in which the dominant ionization process for all the ions we consider is photoionization from the ground state. Furthermore, we neglect recombinations from excited states such that the condition of ionization equilibrium can be expressed as

$$n_{i,0} \gamma_{i,0} = n_e n_{i+1,0} \sum_l \alpha_{i+1,0 \rightarrow l}, \quad (5)$$

where $n_{i,0}$ is the atomic level population of an ionization state i in its ground state (denoted 0), n_e is the free electron density, $\gamma_{i,0}$ is the photoionization rate coefficient from the ground state of ion i and $\alpha_{i+1,0 \rightarrow l}$ is the recombination rate coefficient from the ground state of ionization state $i+1$ to level l of ionization state i . The summation runs over all states of the lower ion.

This can be rewritten as

$$\frac{n_{i+1,0} n_e}{n_{i,0}} = \zeta(T_e) S_i(T_e, J_v) \Phi_{0,0,i}(T_e), \quad (6)$$

where $\Phi_{0,0,i}(T_e)$ is the population ratio $n_{i+1,0} n_e / n_{i,0}$ evaluated for LTE at the electron temperature (T_e) and

$$\zeta = \frac{\alpha_{i+1,0 \rightarrow 0}}{\sum_l \alpha_{i+1,0 \rightarrow l}} \quad (7)$$

is the fraction of recombinations that go directly to the ground state.

$$S_i(T_e, J_v) = \frac{\gamma_i}{\gamma_i^{\text{LTE}}} = \frac{\int_{\nu_0}^{\infty} a_\nu J_\nu \nu^{-1} d\nu}{\int_{\nu_0}^{\infty} a_\nu B_\nu(T_e) \nu^{-1} d\nu} \quad (8)$$

is the ratio of the true photoionization rate determined from the mean intensity (J_ν) and that which would be obtained in LTE at T_e . a_ν is the ground-state photoionization cross-section for frequency ν , B_ν is the Planck function and the integrations run from the threshold frequency, ν_0 , to infinity.

Equation (6) is used for all the ionization calculations in this paper. Since $\Phi_{0,0,i}$ and ζ depend only on the adopted electron temperature these can be evaluated prior to the MC radiative transfer simulation. S_i , however, depends on the radiation field J_ν and so it is computed from the radiation field parametrization and iterated (see Section 3.4).

2.5.2 Excitation

Since the majority of the atomic processes with which we are concerned are associated with ground-state absorption, the treatment of excited level populations is relatively unimportant and therefore very approximate. For all excited states, we adopt a two-level radiation-dominated Sobolev approximation

$$\frac{n_l}{n_0} = \frac{g_l}{g_0} \left(\frac{2h\nu_l^3 \bar{\beta}}{\bar{J}_\nu c^2} + 1 \right)^{-1}, \quad (9)$$

where $h\nu_l$ is the excitation energy of state l above the ground state, g_l is the statistical weight of level l , $\bar{\beta}$ is the angle-averaged Sobolev escape probability for the transition from level l to the ground state and \bar{J}_ν is the mean intensity in the transition.

3 RADIATION TRANSPORT SIMULATIONS

The propagation of radiation through the model is followed via an MC simulation in which the quanta are indivisible packets of radiative energy. The principles of the method have been developed and described elsewhere (e.g. Abbott & Lucy 1985; Lucy & Abbott 1993; Mazzali & Lucy 1993; Lucy 2002, 2003) so only those points of specific relevance to the procedure used in this study are given below.

3.1 Computational grid

For the radiative transfer calculations, the wind properties are first discretized on to a grid in the natural wind parameters (R , l). Typically a 100×100 grid is used. For convenience when propagating the packets, this grid of wind properties is then mapped to an underlying 3D Cartesian grid, typically $100 \times 100 \times 100$. Each Cartesian cell which lies inside the wind is assigned the density, ionization/excitation state and radiation field properties of the closest point in the grid of wind properties while those Cartesian grid cells which lie outside the wind are assumed to be empty.

3.2 Initialization of packets

Since our primary objective is to simulate spectra in the keV energy range, we initially create packets between 0.1 and 40 keV. A power-law distribution of packet energies is assumed such that the input spectrum $n(E)$ varies with photon energy (E) according to

$$n(E)(\text{photons s}^{-1} \text{ keV}^{-1}) \propto E^{-\Gamma}. \quad (10)$$

This is an adequate first-order description of the observed X-ray spectra of AGN in the 2–10 keV range with which we are primarily concerned. The power-law index (Γ) is an input parameter for our model.

It is assumed that the primary X-ray source is compact and roughly appears as a point source as seen from the outflowing gas. Thus, the packets are launched from the coordinate origin. Their initial directions are chosen isotropically.

3.3 Propagation of packets

Once launched, the packets propagate until they reach the outer boundary of the computational domain. As they propagate, the packets can interact with the outflowing plasma, thereby changing both their direction of propagation and their observer-frame frequency. In all interactions, energy conservation is strictly enforced such that, in a local comoving frame, there is no net gain or loss of radiative energy. The particular types of packet interaction which may occur during the simulation are summarized below.

3.3.1 Compton scattering

By far the most common interaction is Compton scattering by free electrons. This process is treated using the method outlined by Lucy (2005). In all our simulations, we assume the electron temperature is small enough that inverse Compton scattering may be neglected in the comoving frame.

3.3.2 Photoabsorption

Bound-free continua can absorb any photons with frequency above their edges – the cross-sections are obtained from the atomic data

sources described in Section 3.5. During the MC simulations, only bound-free absorption by ionic ground states is included.

3.3.3 Bound-bound absorption

Atomic lines can absorb photons that come into resonance with them. Their optical depths are computed in the Sobolev approximation using the velocity gradient and the appropriate level populations obtained from the ionization/excitation formulae.

3.3.4 Re-emission

Following photoabsorption or bound-bound absorption, the macro-atom scheme devised by Lucy (2002, 2003) is used to determine the subsequent re-emission frequency of the packet. This approach naturally incorporates both resonance scattering and line emission following recombination, the two processes which are of greatest interest for outflow features in AGN X-ray spectra. The particular macro-atom scheme adopted allows for bound-bound radiative and electron collisional processes in both internal state changes and deactivation. Bound-free recombination processes are also included but, in accordance with the assumption made for equation (6), photoionization from excited states is neglected.

Packets emitted by macro-atoms via bound-free continua are radiated isotropically. For bound-bound transitions, the direction of re-emission is determined by constructing a 2D grid of Sobolev escape probabilities as a function of polar and azimuthal angle and sampling this distribution to choose a new packet trajectory.

3.3.5 k -packets

When the outcome of an interaction is a conversion of a radiative packet to a packet of thermal energy (k -packets in the nomenclature of Lucy 2003), we assume that the subsequent elimination of the k -packet predominantly leads to emission at lower photon energies such that these packets are lost to the hard X-ray energy band.

3.4 Monte Carlo estimators and the radiation field

3.4.1 Parametrization of the radiation field

The treatment of ionization requires that the radiation field be known locally. Since the wind may be optically thick, the radiation field is computed from the behaviour of the MC packets using volume based estimators. In principle, it is possible to describe an arbitrary radiation field using MC estimators for the mean intensity in narrow frequency bins. However, this requires very large numbers of MC quanta which becomes restrictive for the exploration of model parameter spaces. Therefore, we follow previous MC studies in adopting a physically motivated parametrization of the radiation field.

This method has been described by Lucy (1999, 2003, 2005) and used in various other studies (e.g. Mazzali & Lucy 1993; Long & Knigge 2002). In these previous studies, it was assumed that the true radiation field was blackbody in character and was therefore usually parametrized by a radiation temperature and a dilution factor. Here, however, we are concerned with a radiation field which is non-thermal in character and so parametrization based on a power law is adopted:

$$J_\nu(r) = W(r)v^{\alpha(r)}, \quad (11)$$

where both the parameters W and α are functions of position. Given our choice of input radiation field equation (10), if the wind is optically thin, we would expect to have $\alpha(r) = 1 - \Gamma$ at all points. However, for optically thick winds, we expect variation in α . Using this description, the S_i factors in the ionization equation can be expressed as functions of only T_e and the local values of W and α :

$$S_i(T_e, W, \alpha) = \frac{W \int_{v_0}^{\infty} a_v v^{\alpha-1} dv}{\int_{v_0}^{\infty} a_v B_v(T_e) v^{-1} dv}. \quad (12)$$

This allows the ionization state of the gas to be uniquely determined from T_e , the local mass density and the radiation field parameter pair $[W, \alpha]$ only.

To specify the excitation state via equation (9), we also need to know \bar{J}_v for ground-state transitions. Again, exact MC estimators for \bar{J}_v in all transitions can be constructed but recording and storing them for large numbers of transitions in multidimensional grids becomes expensive in terms of both processor time and memory allocation. \bar{J}_v can be expressed as

$$\bar{J}_v = \frac{1}{4\pi} \int_0^{2\pi} \int_{-1}^1 I_{v,\mu,\phi} \beta_{\mu,\phi} d\mu d\phi, \quad (13)$$

where $\cos^{-1} \mu$ and ϕ are spherical polar angles, $I(v, \mu, \phi)$ is specific intensity and $\beta(\mu, \phi)$ is the Sobolev escape probability for the transition. For the specific case of a homologous flow, β becomes independent of direction but, in general, it is a function of both μ and ϕ . In the interests of computational expediency, however, we neglect this dependency and replace $\beta_{\mu,\phi}$ with its angle-averaged value, $\bar{\beta}$. This simplification allows \bar{J}_v to be expressed as

$$\bar{J}_v = \frac{1}{4\pi} \bar{\beta} \int_0^{2\pi} \int_{-1}^1 I_{v,\mu,\phi} d\mu d\phi = \bar{\beta} J_v = W v^\alpha \bar{\beta}, \quad (14)$$

adopting our parametrization of the radiation field. This simplifies equation (9) to give our final excitation formula

$$\frac{n_l}{n_0} = \frac{g_l}{g_0} \left(\frac{2h}{W v_l^{\alpha-3} c^2} + 1 \right)^{-1}, \quad (15)$$

where $h\nu_l$ is the excitation energy of state l above the ion ground state. This treatment of excitation avoids the need to specify any radiation field parameters beyond those used in the ionization formula and therefore places no further computational demands on the MC simulations. It is very crude but is not of critical importance to our study of highly ionized outflows since the excitation state is low enough that the ground-state populations of H- and He-like species are dominant. The most important failing of this treatment will be for the metastable triplet states of He-like ions. Thus improvements to the treatment of excitation will be necessary in order to extend the code for applicability to less ionized flows and softer wavebands.

3.4.2 Monte Carlo estimators

The values of W and α are obtained by recording two MC estimators per grid cell:

$$E_n^{(1)} = \sum_{\text{paths in } n} \epsilon_{\text{cmf}} ds, \quad (16)$$

$$E_n^{(2)} = \sum_{\text{paths in } n} \epsilon_{\text{cmf}} \nu_{\text{cmf}} ds, \quad (17)$$

where the summation runs over all quanta trajectories which lie inside the grid cell of interest (denoted by n) and in which the packet frequency lies in the regime of interest ($\nu_{\min} < \nu < \nu_{\max}$). In

these equations, ds is the length of an MC quanta trajectory length, ϵ_{cmf} is the comoving frame packet energy and ν_{cmf} is the comoving frame packet frequency.

Values for $E_n^{(1)}$ and $E_n^{(2)}$ are recorded during the MC simulation of all the packets. At the end of the simulation, they are used to obtain values of α_n and W_n in each grid cell as follows.

The ratio $E_n^{(2)}/E_n^{(1)}$ gives the mean frequency. Since we know the frequency interval being simulated ($\nu_{\min} < \nu < \nu_{\max}$), this ratio is directly linked to the power-law index via

$$\frac{E_n^{(2)}}{E_n^{(1)}} = \frac{\alpha_n + 1}{\alpha_n + 2} \frac{\nu_{\max}^{\alpha_n+2} - \nu_{\min}^{\alpha_n+2}}{\nu_{\max}^{\alpha_n+1} - \nu_{\min}^{\alpha_n+1}} \quad (18)$$

which can be numerically solved for α .

Once α_n is known, W_n can be obtained by normalizing $E_n^{(1)}$:

$$W_n = \frac{E_n^{(1)}}{4\pi V_n \Delta t} \frac{\alpha_n + 1}{\nu_{\max}^{\alpha_n+1} - \nu_{\min}^{\alpha_n+1}}, \quad (19)$$

where V_n is the volume of grid cell n and Δt is the effective time interval represented by the MC simulation.

3.4.3 Iteration

The formulae given above allow values of W_n and α_n to be obtained from the behaviour of the MC quanta. However, since the values of these parameters also affect the MC simulation (primarily owing to their importance in determining the ionization state), these parameters must be iterated to reach a converged parametrization of the radiation field.

In practice, the radiation field parameters are found to converge very rapidly, often requiring only one iteration step.

3.5 Atomic data

Table 1 lists the elements and ionization stages that are included in the radiative transfer calculations; for all the light elements, only the highest three ionization stages are included while for Fe and Ni the five highest stages are treated.

The solar element abundances of Asplund, Grevesse & Sauval (2005) are adopted.

For all elements other than Fe, atomic models, bound-bound oscillator strengths and electron collision rates were extracted from the CHIANTI atomic data base, version 5 (Dere et al. 1997; Landi et al. 2006). These data include levels with principal quantum number $n \leq 5$ for the H-like ions and for states up to the $1s5g$ configuration for He-like ions. Ni xxv and Ni xxvi are included only for the calculation of the ionization balance; currently no bound-bound transitions for these ions are treated.

For Fe, atomic data were taken from TIPBASE¹ which provides atomic data from the IRON project for ions of astrophysical interest. These data also contain levels for $n \leq 5$ of Fe xxvi but include more highly excited configurations of Fe xxv than CHIANTI (up to the $1s10h$ configuration). Atomic data for Fe xxiii and Fe xxiv were also taken from TIPBASE; however, no states involving excitation of electrons from the $1s$ shell are included for either of these ions.

Ground configuration photoionization cross-sections were described by the fits from Verner et al. (1996), except for Ni for which fits from Verner & Yakovlev (1995) were adopted. For excited states, photoionization cross-sections were computed using a hydrogenic approximation for all ions. Since bound-free absorption

¹ <http://vizier.u-strasbg.fr/tipbase/home.html>.

Table 1. Elements and ions which are included in the radiative transfer calculations.

Element	Ions	Element	Ions
C	V–VII	S	XV–XVII
N	VI–VIII	Ar	XVII–XIX
O	VII–IX	Ca	XIX–XXI
Ne	IX–XI	Fe	XXIII–XXVII
Mg	XI–XIII	Ni	XXV–XXIX
Si	XIII–XV		

from excited states was not included in the MC simulations, these excited state cross-sections are only needed for the computation of macro-atom transition probabilities (see Section 3.3.4). The fraction of recombinations which go directly to the ground state, ζ , was obtained from the hydrogenic calculations of Martin (1988).

4 EXAMPLE CALCULATION

In this section we present detailed results pertaining to one particular instance of our model.

4.1 Model parameters

The complete set of adopted input parameters for our example model is given in Table 2.

The black hole mass, source X-ray luminosity and primary power-law index are all chosen to be reasonable for Mrk 766, the object for which we make a detailed comparison in Section 8 [$M_{\text{bh}} \sim 4.3 \times 10^6 M_{\odot}$ (Wang & Lu 2001); $L_X \sim 10^{43} \text{ erg s}^{-1}$ (Pounds et al. 2003b); $\Gamma \sim 2.38$ (Miller et al. 2007)]. We assume that $f_v = 1$, which is characteristic of radiatively driven flows. Furthermore, since we wish to consider outflow features with shifts corresponding to $v_{\infty} \gtrsim 0.1c$, we require flow launching radii $\lesssim 200r_g$ – hence we adopt $r_{\text{min}} = 100r_g$ and $r_{\text{max}} = 150r_g$.

Physically, R_v and β should depend on the acceleration mechanism and location – however, since such properties are unknown, we

Table 2. Inputs parameters for the example model. The upper portion gives the adopted physical parameters and the lower portion gives numerical parameters.

Parameter	Value
Radiative source luminosity (2–10 keV), L_X	$10^{43} \text{ erg s}^{-1}$
Source power-law photon index, Γ	2.38
Mass of central object, M_{bh}	$4.3 \times 10^6 M_{\odot}$
Inner launch radius, r_{min}	$100 r_g = 6.4 \times 10^{13} \text{ cm}$
Outer launch radius, r_{max}	$1.5 r_{\text{min}}$
Distance to wind focus, d	r_{min}
Terminal velocity parameter, f_v	1.0
Velocity scalelength, R_v	r_{min}
Velocity exponent, β	1.0
Launch velocity, v_0	0.0
Wind mass-loss rate, \dot{M}	$0.1 M_{\odot} \text{ yr}^{-1}$
Mass-loss exponent, k	−1.0
Electron temperature, T_e	$3 \times 10^6 \text{ K}$
Extent of grid	$2 \times 10^{15} \text{ cm}$
3D Cartesian RT grid size	$100 \times 100 \times 100$
2D wind grid	100×100
Number of MC quanta	2.4×10^8

adopt $R_v = r_{\text{min}}$ and $\beta = 1$, as appropriate for the simple case of an acceleration which occurs on the scale of the system. It is assumed that $v_0 \ll v_{\infty}$ such that $v_0 = 0$ can be adopted in the numerical simulations.

For the example model, we adopt a polar opening angle of 45° (i.e. $d = r_{\text{min}}$), a moderate mass-loss rate ($\dot{M} = 0.1 M_{\odot} \text{ yr}^{-1}$) and electron temperature $T_e = 3 \times 10^6 \text{ K}$. The effects of varying these parameters will be discussed in Section 5.

4.2 Computed ionization state

The ionization state is very important since it determines the distribution of line opacity within the outflow. Fig. 2 shows the computed ionization fraction of Fe K-shell ions (i.e. Fe xxv + Fe xxvi) in the example model.

There is significant variation in the ionization state in the wind. The surface of the outflow closest to the rotation (z) axis is most highly ionized since it sees unattenuated X-ray radiation from the continuum source. In the outermost parts of the wind the ionization state is high and relatively uniform: although far from the X-ray source, these regions have low density which disfavours recombination. Across the wind, there is a significant ionization gradient since each layer progressively shields those below it from the X-ray source. The very lowest ionization material occurs near the xy plane on the outer edge of the wind – this region has both the highest densities and the most effective shielding from the X-ray source.

4.3 Computed spectra

Fig. 3 shows spectra computed for the example model. These were obtained by binning the emergent MC quanta by angle relative to the polar axis (θ). The first eight angular bins shown each cover equal solid angle, specifically they encompass $\Delta \cos \theta = 0.1$ while the ninth covers the equatorial range $0 < \cos \theta < 0.2$.

During the MC simulations, the number of interactions was recorded for each quantum. This information has been used to divide the spectra into ‘direct’ (meaning quanta which underwent no interactions) and ‘scattered’ components (note that this includes packets that underwent *any* number of *any* type of physical event – it does not only include true scattering events). These component spectra are also plotted in the figure.

It is apparent that the outflow in the example model affects the spectrum as observed from any line of sight. The typical apparent luminosity varies by more than a factor of four – the flux level is much higher close to the polar axis than near the equatorial plane. This is a consequence of scattering in the flow, primarily by free electrons. For small angles relative to the polar axis the source radiation escapes directly, unhindered by the wind. At high inclination angles, the photons enter the wind and most are scattered, thereby changing their direction of propagation. Compared to the naked source, this enhances the radiation for the polar direction and suppresses it close to the equator. Also, as one would expect, the scattered radiation field is softer than the direct such that the combined spectrum is also slightly softer.

For viewing angles less than 45° the spectrum is unobscured by the outflow and is supplemented by scattered radiation which, for this model, can have more than 50 per cent as high a flux as the direct component. These lines of sight are indicated by the solid lines in Fig. 2 and the corresponding spectra are shown in the top three panels of Fig. 3. The scattered radiation field shows signatures of scattering in spectral lines – a P-Cygni-type line profiles is apparent

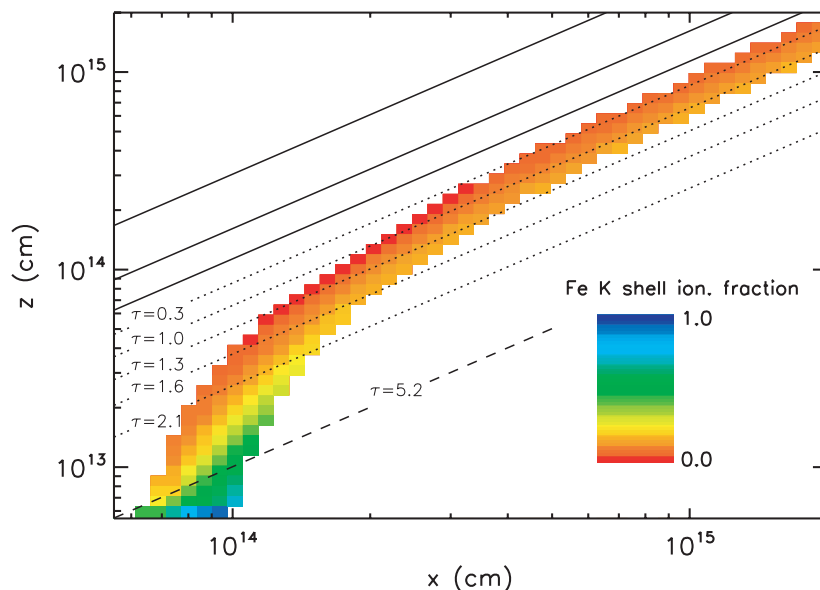


Figure 2. The computed ionization fraction for K-shell Fe (i.e. Fe xxv + Fe xxvi). Only the positive xz plane is shown. Note the logarithmic axes and the difference in scalefactor on the x - and z -axes. The blue–red colours indicate the ion fraction on a linear scale – red shades represent regions where the wind is almost fully ionized (i.e. Fe xxvii is dominant). The black lines indicate lines of sight from the X-ray source (the coordinate origin); the lines of sight drawn are those at the mid-points of the nine angular bins used for the spectra shown in Fig. 3. The solid lines are lines of sight that never intersect the outflow (corresponding to the top three panels in Fig. 3); the dotted lines intersect the outflow and yield spectra with narrow absorption features (fourth to eighth panels in Fig. 3); the dashed line intersects the outflow and produces a spectrum without narrow absorption features (last panel in Fig. 3). The lines of sight which intersect the flow are labelled with their integrated Compton optical depth (τ) from the continuum source (coordinate origin) to the observer.

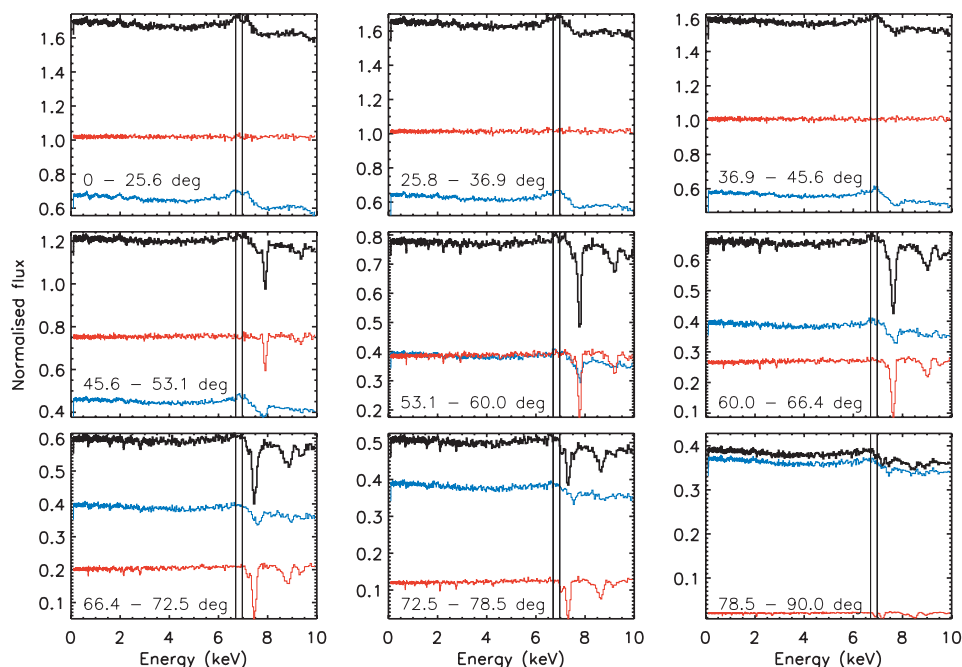


Figure 3. Spectra computed for the example model for different lines of sight. Each panel shows the spectrum in a different inclination angle bin (the angular bin sizes are indicated in the figure, measured relative to the polar axis). Note that the ordinate range is different in each panel and does not extend to zero. The total spectrum is plotted in black. The spectrum is separated into direct and scattered components and these are overplotted in red and blue, respectively. All the spectra are shown normalized to the input primary power-law spectrum. The solid vertical lines indicate the rest energies of Fe $K\alpha$ for the Fe xxv and Fe xxvi ionization stages.

in the Fe $K\alpha$ line and there are weaker but similar features arising from the $K\alpha$ lines of lighter elements at softer energies.

At intermediate viewing angles (dotted lines of sight in Fig. 2), the line of sight intersects the flow. The Compton optical depth

along these sight lines (τ) is of the order of unity (see labels in Fig. 2) meaning that a significant fraction of the continuum radiation emitted in these directions is scattered by the flow. Discrete narrow blueshifted absorption lines appear in these spectra (fourth to eighth

panels of Fig. 3). The blueshift which manifests in any particular spectrum depends on the component of outflow velocity which lies along the line of sight and hence on the inclination. In our model, the blueshift increases as θ decreases. The scattered component also contains absorption features, albeit weaker and broader than those in the direct spectrum. In addition, it includes emission which results from line scattering throughout the model and is thus significantly velocity broadened.

When viewed from high inclination angle (dashed line of sight in Fig. 2 and last panel of Fig. 3), the flow is significantly optically thick and the spectrum is totally dominated by scattered radiation. These spectra show weak emission lines and weak, relatively broad absorption lines.

Thus our example model demonstrates that the simple disc wind geometry adopted can naturally produce narrow, blueshifted absorption features, as required. However, it also makes clear that such features are not necessarily produced and that depending on the inclination angle a variety of other features, including relatively broad emission or absorption, may be present.

In the example model, the greatest contrast of the line features to the continuum, is only about 40 per cent. There are lines of sight (e.g. $\theta \sim 75^\circ$) in which the direct component shows narrow absorption features which are close to black at line centre. However, in the total spectrum the contrast is always reduced by addition of the scattered component in which all features are smeared by velocity broadening. We note that our assumption of a stationary, smooth flow is likely to maximize this effect since it will generally overestimate the relative strength of scattered to direct radiation for lines of sight in which absorption features occur.

5 MODEL GRID

Having discussed the complete spectra from the example model (Section 4), we now explore the effects of some critical model parameters on the computed spectra. To do this we have constructed a grid of 45 models and computed spectra for each in 10 viewing-angle bins. The parameters which were varied between models, and their respective effects on the spectrum, are discussed in the sections below.

In order to elucidate our discussion, we have performed simple measurements of the properties of the Fe K absorption features in the spectra. First, for each spectrum a continuum spectrum was obtained by masking out the strong K α absorption lines and then median filtered to suppress MC noise. The equivalent width (EW) of any Fe K α absorption was then measured by numerical integration of the normalized spectrum. The spectra with absorption EWs > 40 eV were then classified by eye into one of three categories:

- (i) spectra with a single, clear Fe K α absorption line;
- (ii) those having two, well-separated Fe K α absorption lines (one due to Fe xxv and the other due to Fe xxvi);
- (iii) those with K α absorption in both Fe xxv and Fe xxvi but in which the two lines are strongly blended.

For the lines in categories (i) and (ii), the blueshift line velocity was found by measuring the photon energy of deepest absorption and an approximate full width at half-maximum (FWHM) was determined for the absorption feature by fitting a Gaussian profile. For the spectra in class (iii), Fe K α velocities and FWHM were not extracted. Although these line properties do not adequately describe all properties of the spectra, they provide a convenient quantification of the spectra for the discussions in the sections below.

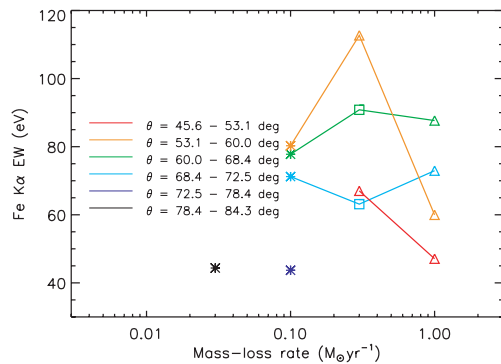


Figure 4. Fe K α absorption EWs for models with different \dot{M} values (all other parameters held fixed). The star, triangle and box symbols indicate spectra in which there is a single, clear Fe K α absorption line, those in which there is a pair of separated Fe K α lines and those in which the Fe xxvi and Fe xxv components are strongly blended, respectively. The colours identify spectra based on the inclination of the observer line of sight to the polar axis (θ). Note that only spectra with Fe K α absorption EWs > 40 eV are included.

5.1 Mass-loss rate, \dot{M}

The wind mass-loss rate is the most important model parameter which one would wish to constrain observationally. To demonstrate its effect, we have computed spectra for models with five \dot{M} values (0.01, 0.03, 0.1, 0.3 and $1.0 M_\odot \text{ yr}^{-1}$); the Fe K α absorption EWs for these models are shown in Fig. 4. For Mrk 766, this range of mass-loss rates explores the region around the mass accretion rate estimated from the bolometric luminosity $\dot{M}_{\text{acc}} \approx L_{\text{bol}}/0.054c^2 \sim 0.1 M_\odot \text{ yr}^{-1}$ adopting the bolometric luminosity ($L_{\text{bol}} = 3 \times 10^{44} \text{ erg s}^{-1}$) from Hao et al. (2005) and the radiative efficiency for a Schwarzschild black hole (Shapiro & Teukolsky 1983).

\dot{M} controls the density in the wind and therefore affects both the ionization state and all line or continuum optical depths. At the low end of our parameter range, the ionization state is high enough that absorption by Fe xxvi is much more important than Fe xxv. Increasing \dot{M} leads to an increase in absorption EWs, as one would expect from the increase in opacity. Also for small \dot{M} , strong absorption is only present at large θ since only the very base of the flow is dense enough to present significant opacity.

At intermediate \dot{M} , absorption appears across a wider range of θ and becomes generally stronger. Increased densities reduce the degree of ionization such that absorption by both Fe xxv and Fe xxvi K α becomes more common. Absorption at very high inclination angles becomes less significant since at these angles, the spectra are increasingly dominated by scattered radiation which washes out any narrow absorption features imprinted on the direct radiation.

For the highest mass-loss rates considered, all the spectra contain absorption by both Fe xxvi and Fe xxv K α and scattered emission is very important at all inclination angles. This means that the EWs are mostly lower in the $\dot{M} = 1$ than $0.3 M_\odot \text{ yr}^{-1}$ spectra.

5.2 Wind geometry, d

Within our simple wind prescription, d controls the opening angles of the outflow and therefore determines both the angular range of lines of sight which pass through the wind and the relative orientations of the outflow and rotational velocity fields. To explore the effect of geometry on the spectrum, we have extended our grid of

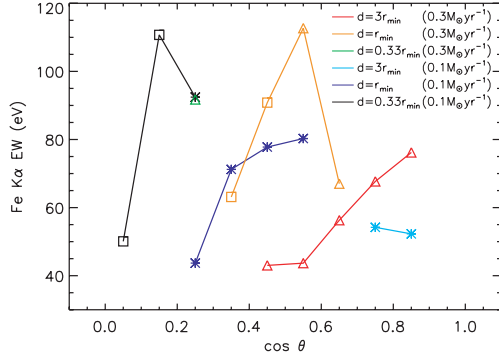


Figure 5. Fe K α absorption EWs versus line-of-sight inclination for models with different d and \dot{M} values (all other parameters held fixed). The plotting symbols are as described for Fig. 4. Note that only spectra with Fe K α absorption EWs > 40 eV are included.

models to include d values of 0.33 and $3r_{\min}$, thereby producing geometries which are, respectively, more equatorial and more polar than the example model. For these d values, we have computed models with the same set of \dot{M} values used in Section 5.1, keeping all other parameters fixed to those of the example model.

Fe K α absorption EWs are plotted for a sample of these models in Fig. 5. This shows the role of the wind opening angles in determining which lines of sight intersect the outflow in regions where optical depths are high enough to cause line absorption.

The wind opening angles and line-of-sight orientation also affect the observed Fe K α blueshift. Fig. 6 shows the Fe xxvi blueshift velocity for the same models used in Fig. 5, excluding spectra with blended Fe xxv and xxvi K α absorption. As mentioned in Section 4, the variation in blueshift arises from line-of-sight projection of the outflow velocity and the effect is large: there can be more than a factor of two spread in the apparent blueshift. Since the maximum outflow velocity is

$$v_{\infty} = \sqrt{\frac{2GM_{\text{bh}}}{r_{\min}}} = 0.14c = 4.2 \times 10^4 \text{ km s}^{-1} \quad (20)$$

for all the models discussed here, the variation in blueshift is entirely a consequence of orientation. Thus, while the apparent blueshift can be as large as the terminal outflow velocity, it is often significantly smaller.

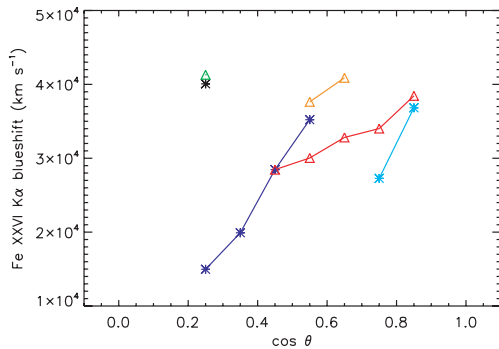


Figure 6. The blueshift of the Fe xxvi K α line versus line-of-sight inclination for models with different d and \dot{M} values. The plotting symbols and colours are as described for Fig. 5. Note that only spectra with Fe K α absorption EWs > 40 eV are included.

5.3 Inner launch radius, r_{\min}

The inner launch radius of the wind, r_{\min} , determines how far the wind material is from the X-ray source and affects the wind density since the surface area of annuli in the disc plane increases with r . To investigate its effect, we have computed spectra for models with r_{\min} larger than in the standard model ($r_{\min} = 200 r_g$ and $500 r_g$) adopting the same range of \dot{M} values used in Section 5.1. For all these models, we also varied other parameters as necessary to preserve the relationships used for the standard model (i.e. $r_{\max} = 1.5r_{\min}$; $d = r_{\min}$; $R_v = r_{\min}$, $f_v = 1$). Fig. 7 shows Fe K α absorption EWs computed as a function of viewing angle for six of these models.

Changing r_{\min} affects the typical range of viewing angle for which absorption features are strong, favouring smaller $\cos \theta$ for larger r_{\min} . For fixed \dot{M} , increasing r_{\min} tends to make the absorption lines weaker, a consequence of the reduced density in the flow.

5.4 Electron temperature, T_e

Under our assumptions, the only important role played by the electron temperature is in determining the ionization fractions. To illustrate its effect, we have used models which span the same \dot{M} grid as discussed in the section above but which adopt T_e both lower (10^6 K) and higher (10^7 K) than used in the example model. EWs for a subset of these models, namely all those having $\dot{M} = 0.1 M_{\odot} \text{ yr}^{-1}$ are shown in Fig. 8.

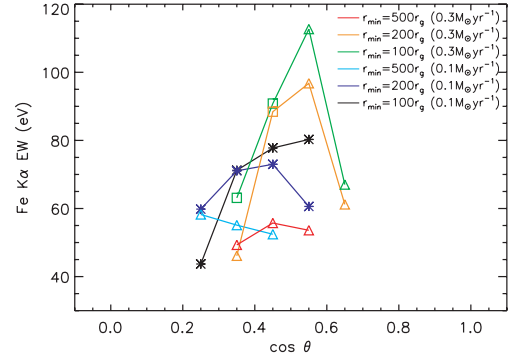


Figure 7. Fe K α absorption EWs versus line-of-sight inclination for models with different r_{\min} and \dot{M} values. The plotting symbols are as described for Fig. 4. Note that only spectra with Fe K α absorption EWs > 40 eV are included.

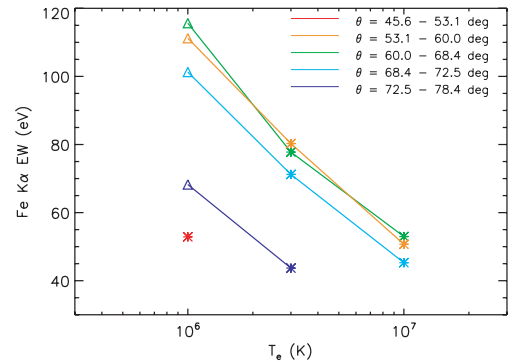


Figure 8. Fe K α absorption EWs for models with different T_e values (all other parameters held fixed). The plotting symbols are as described for Fig. 4. Note that only spectra with Fe K α absorption EWs > 40 eV are included.

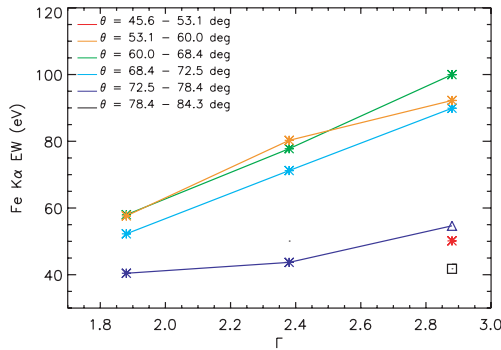


Figure 9. Fe K α absorption EWs for models with different Γ values (all other parameters held fixed). The plotting symbols are as described for Fig 4. Note that only spectra with Fe K α absorption EWs > 40 eV are included.

The dependence on T_e of these models is very simple. As T_e increases, the wind becomes more ionized, reducing the H- and He-like ion populations in favour of the fully ionized state. This reduces the line opacities and causes the absorption EWs to decrease. Absorption in both Fe xxv and xxvi is most common at low T_e since the Fe xxv population is depleted more rapidly than that of Fe xxvi as the wind becomes more ionized.

5.5 Primary power-law index, Γ

The source power-law index determines the fraction of the X-ray flux which is hard enough to contribute to the ionization of Fe xxv and xxvi and therefore has an effect on the Fe K α absorption EWs which is qualitatively similar to that of T_e . In Fig. 9 we show Fe K α EWs for models with $\dot{M} = 0.1 M_\odot \text{ yr}^{-1}$ adopting $\Gamma = 1.88, 2.38$ and 2.88 , with other parameters as in the example model. As expected, higher Γ values lead to larger EWs since there are fewer Fe K-shell ionizing photons and hence the ionization state is lower.

Note that the total 2–10 keV luminosity (L_X) is constant here – although we have not explicitly explored the effect of changing L_X , it is clear that it will have a similarly simple effect on the ionization state.

6 OBSERVABLE PROPERTIES

In Section 5 we constructed a grid of models to explore the effects of various wind properties on the Fe K α absorption-line properties. However, since the relevant wind parameters are not known a priori it is instructive to investigate the properties of the models in the space defined by observable quantities. Given the typical data quality and limited spectral resolution of current X-ray telescopes, the primary observables pertaining to K α absorption lines are the EW and the velocity shift of the lines.

Of the 450 spectra which were generated with our grid of models (Section 5), 101 were classified as having Fe K α absorption EWs of > 40 eV and, of these, 79 were classified as having either a single or an unblended pair of absorption features such that a meaningful velocity blueshift could be extracted from the spectrum. Fig. 10 shows the distribution of Fe K α absorption EWs versus the Fe xxvi blueshift for these 79 spectra.

There are a wide variety of K α absorption features in our models. EWs of more than 100 eV are rare but do occur; the maximum EW produced by any of the models is ~ 135 eV. As one would expect, the EW tends to be larger when two lines are present although there are cases where a single line achieves an EW of nearly 100 eV. As

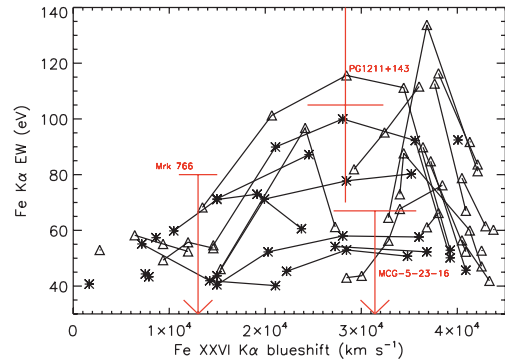


Figure 10. Fe K α absorption EWs versus the Fe xxvi blueshift. All spectra computed from our grid of models (450 spectra in total) with unblended Fe K α absorption with EW > 40 eV are included in the plot. The star symbols represent model spectra in which a single Fe K α absorption line is dominant. Triangles indicate spectra with two, unblended Fe K α absorption lines. The solid lines connect points for the same model but viewed from different inclination angular bins. The red cross indicates the Fe K α absorption line reported by Pounds et al. (2003a) for PG1211+143 while the red bars indicate the range of EWs obtained with the time-sliced observations of Mrk 766 (Turner et al. 2007) and MCG-5-23-16 (Braitto et al. 2007).

already highlighted in Section 5.2, a very wide range of blueshift velocity is predicted. Typically, the maximum EWs is larger when the blueshift is larger; but there is significant variation in EW at all blueshifts. In general, there are many sets of wind parameters that can produce similar EWs and blueshifts such that K α properties cannot uniquely discriminate between our models. Other potential outflow signatures are discussed in Section 7.

As a simple comparison, points representing reported detections of narrow blueshifted K α absorption in the spectra of three real AGN (PG1211+143, Mrk 766 and MCG-5-23-16; see below) are overplotted in Fig. 10. Observations clearly show that outflow absorption features are significantly time variable (e.g. Risaliti et al. 2005; Braitto et al. 2007; Miller et al. 2007; Turner et al. 2007) and thus one must be cautious when comparing them directly to the results of our steady-state models – the development of multidimensional models involving clumpy or structured flows is necessary for a detailed comparison.

Pounds et al. (2003a) first reported blueshifted K α absorption from H- or He-like Fe in the spectrum of PG1211+143 (see also Pounds et al. 2005; Pounds & Page 2006; Pounds & Reeves 2007 for further discussion of this interpretation of the PG1211+143 spectrum); they report an absorption EW of 105 ± 35 eV (Pounds et al. 2005) and a blueshift of either 0.08–0.10c (Pounds et al. 2005) or 0.13–0.15c (Pounds & Page 2006), depending on whether one assumes the observed features is owing to Fe xxvi or xxv. The point plotted in Fig. 10 for this object assumes the Fe xxvi interpretation and the measurement uncertainties quoted by Pounds et al. (2005).

Two distinct absorption features (6.9 and 7.2 keV) were reported in spectra of Mrk 766 (Miller et al. 2007; Turner et al. 2007), at 6.9 and 7.2 keV. Although the nature and relationship between these features is unclear, one possible interpretation is that they correspond to blueshifted absorption by Fe xxv and Fe xxvi, respectively – in this case, the blueshift velocity of both lines is $\sim 13\,000 \text{ km s}^{-1}$ (Miller et al. 2007). Turner et al. (2007) showed that the strength of these features varies significantly in time. The largest fluxes of the absorption features occurred in their time-slice 9 (see their fig. 2) and had an EW ~ 80 eV each. In some time-slices, the line fluxes are consistent with zero. In Fig. 10, the range of Mrk 766 absorption

feature properties is marked adopting the $13\,000\text{ km s}^{-1}$ outflow interpretation (i.e. identifying the 7.2-keV feature with Fe xxvi) and the EW range of 0–80 eV as motivated by the time-sliced data.

Braito et al. (2007) detected a variable absorption feature at 7.7 keV in the spectrum of MCG–5-23-16. This feature is also indicated in Fig. 10, adopting the upper bound of on its EW range based on their analysis of the one of five 20-ks time intervals in which the line was most clearly detected (see their table 4). The velocity shift was computed assuming that Fe xxvi is dominant.

In terms of shift and range of EW, the absorption features in PG1211+143, Mrk 766 and MCG–5-23-16 lie close to the space explored by our grid of models (Fig. 10). Thus wind models such as those we have investigated are promising starting points for explaining the K α absorption in these observations.

Blueshifted K α absorption features have also been reported in NGC 1365 (Risaliti et al. 2005). In this case, the shifts are considerably smaller, $\sim 5000\text{ km s}^{-1}$ at most. Although our grid of models does include some spectra with features at these low velocities (see Fig. 10), the EWs in the computed spectra are below those observed by a significant factor (the combined Fe K α EWs reported by Risaliti et al. 2005 are in the range 200–300 eV, lying off the scale of Fig. 10). Even lower blueshift highly ionized absorption has been reported in MCG–6-30-15 (Young et al. 2005; Miniutti et al. 2007; Miller, Turner & Reeves 2008) and NGC 3516 (Turner et al. 2008). The simplest way in which such strong, relatively low-velocity features might be produced with our model would be by considering lower terminal flow velocities but it may also be possible to obtain deeper absorption by considering flows which are significantly clumped. Detailed study of these possibilities lies beyond the scope of this paper, but we do note that even the NGC 1365 features are within a factor of ~ 5 in EW of those obtained with our grid of models.

In principle, the model spectra indicate that the absorption-line shapes are complex and therefore provide information on the outflow properties. However, given the limited sensitivity and spectral resolution of current X-ray telescopes, determining line shapes is virtually impossible – at best, only a rough limit on the characteristic linewidth is available. For comparison with such limits, Fig. 11 shows the FWHM determined from our spectra (by Gaussian fitting) versus the Fe xxvi blueshift for the same models as plotted in Fig. 10.

The FWHM varies between about 3.5×10^3 and $1.8 \times 10^4\text{ km s}^{-1}$, with values around $5\text{--}7 \times 10^3\text{ km s}^{-1}$ being most common. For all our model spectra in which the blueshift is greater than 10^4 km s^{-1} , the FWHM is smaller than the blueshift meaning that the absorption does not extend down to the rest energy of the line.

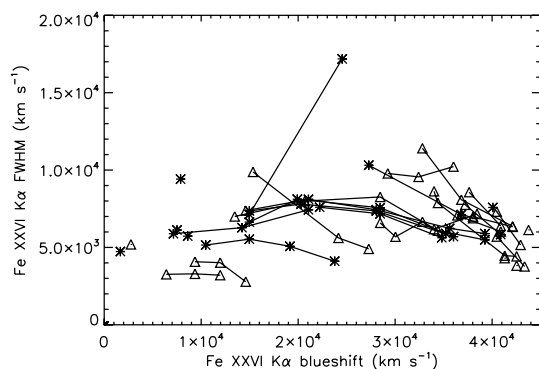


Figure 11. Fe K α FWHM versus the Fe xxvi blueshift. The plot symbols are the same as in Fig. 10.

As one would expect, the largest linewidth ($\sim 1.8 \times 10^4\text{ km s}^{-1}$) occurs in model where d has the smallest value considered ($d = 0.33 r_{\text{min}}$) and for a viewing direction which has a large path-length through the flow.

To our knowledge, there are currently no firm measurements of linewidths for narrow blueshifted Fe K α absorption features in AGN spectra. For PG1211+143, Pounds et al. (2003a) placed a limit of $<1.2 \times 10^4\text{ km s}^{-1}$ on the Fe K α linewidth, which is consistent with the majority of the measurements from our spectra shown in Fig. 11. Braito et al. (2007) found a best-fitting linewidth of $\sigma = 200 \pm 100\text{ eV}$ (FWHM $= 1.8 \times 10^4\text{ km s}^{-1}$) for the absorption feature in MCG–5-23-16. However, the fit in which they allowed the linewidth to vary was not a significant improvement over that in which they pinned the width at $\sigma = 100\text{ eV}$. Thus, their linewidth constraints are also consistent with the majority of the spectra described by Fig. 11.

7 OTHER SIGNATURES OF A FAST OUTFLOW

As discussed in Section 1, blueshifted Fe K α absorption is the clearest signature of highly ionized outflowing gas and has therefore been the central topic of this paper. However, as mentioned in Section 4, narrow blueshifted Fe K α absorption is neither a necessary consequence nor the only signature of a highly ionized flow. Thus if such outflows are common in the AGN population it is important to consider other effects they may have on X-ray spectra. In this section, we briefly describe some of these effects and their possible implications with reference to our model spectra.

7.1 Blueshifted absorption lines other than Fe K α

Although the Fe K α feature is typically the most prominent absorption line, K α absorption by lighter elements is present in many of the spectra computed from our grid of models, particularly those with high \dot{M} values. The strongest of these K α features are those of S, Si and O – the absorption EWs for these lines are up to 10, 10 and 3 eV, respectively. Their strengths correlate closely with each other and more loosely with the Fe K α feature.

At energies harder than Fe K α , absorption by H-/He-like Ni K α and by Fe K β /K γ occur. Individually, these features are all weaker than Fe K α but they are often blended together producing fairly significant absorption which can extend up to around 10 keV.

These additional absorption lines can provide both confirmation of outflows detected via Fe K α and supplementary constraints on the flow properties. However, their reliability is limited since (i) in our models, they are always weaker and thus harder to detect than Fe K α and (ii) with the exception of the hard energy Ni or Fe K β lines, their identifications are less clear since there are more potential atomic transitions at soft energy. Thus, as diagnostics for highly ionized flows, these lines are always of subordinate value to Fe K α .

7.2 Emission lines and P-Cygni profiles

As pointed out in the example spectra shown in Section 4, the blueshifted absorption lines are often accompanied by broad emission which is centred close to the line rest energy. Since these emission features are formed as a result of line scattering and recombination emission in the outflow, their strength strongly depends on the density of the wind; thus although they are fairly weak in the spectra from the example model, they become more significant in our models with higher mass-loss rates. Reliable predictions

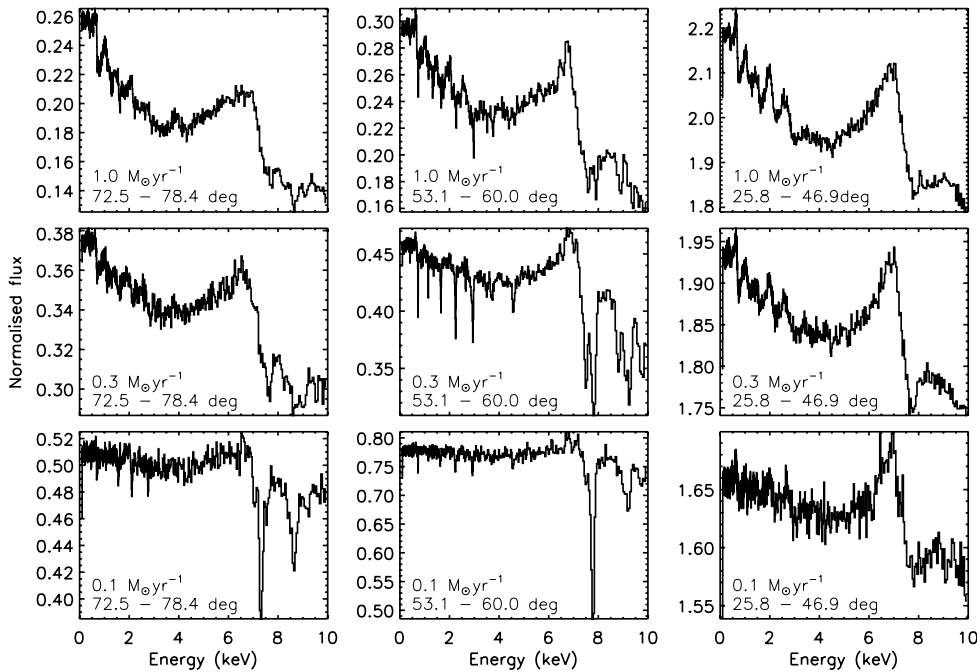


Figure 12. Sample spectra computed for different viewing angle bins (left- to right-hand side) for models with differing mass-loss rates (top to bottom). Except for \dot{M} , all model parameters are fixed at those of the example model. The plotted spectra are all normalized to the input primary power-law spectrum.

for these phenomena in non-spherical outflows require multidimensional radiative transfer and thus our methods are particularly well suited to describing them.

To illustrate the types of line profile, Fig. 12 shows a montage of spectra from models with relatively high mass-loss rates. There is a wide range of $K\alpha$ profile types in these models and their emission EWs, measured relative to a power-law continuum fit, can be in excess of 200 eV; this is comparable to the typical broad $K\alpha$ EWs measured in a sample of AGN by Nandra et al. (2007).

At low inclination angles, our model Fe $K\alpha$ profiles have a near-P-Cygni character: they show some blueshifted absorption and broad, redshifted emission, the strength of which grows with \dot{M} . Such profiles are qualitatively similar to those observed in some Seyfert 1 galaxies (Done et al. 2007).

At intermediate angles, when the line of sight is close to looking down the wind cone, the narrow absorption lines are strongest but are accompanied by moderately strong, emission lines with fairly extended red wings. We note that the narrow absorption lines become less prominent at very high \dot{M} , a consequence of the increased contribution of scattered radiation in the spectra.

For the highest inclinations and \dot{M} values, the Fe $K\alpha$ line is almost pure emission, peaking at the rest energy of the line and having a long red tail. The redward extension of the line emission is not a consequence of gravitational redshift but arises from electron scattering in the outflow.

Although somewhat more diverse, our red-skewed emission-line profile shapes are qualitatively similar to those obtained via the same physical mechanism in spherical outflow models (Laurent & Titarchuk 2007; see also Laming & Titarchuk 2004) while they are significantly broader than those computed by Rózańska & Madej (2008) for Compton scattering in irradiated accretion discs. The largest Fe $K\alpha$ emission EWs found by Laming & Titarchuk (2004) ($\gtrsim 4$ keV) substantially exceed those found in any of our models but we note that the large EWs in their models mostly arise from significantly lower ionization stages than are present in our models.

These emission-line properties show that highly ionized outflows may affect the Fe K region beyond imprinting narrow, blueshifted absorption lines. This may have consequences for study of the Fe K fluorescent emission which originates in AGN accretion discs (e.g. Fabian et al. 1989; Nandra et al. 1997; Fabian et al. 2000; Miller 2007; Nandra et al. 2007), since it may contaminate the disc emission and/or lead to an apparently multicomponent emission line (see e.g. O’Neill et al. 2007). In this context, the red wings predicted for the emission lines may be of particular relevance in view of the potential for confusion with the effects of gravitational redshift – however, more sophisticated 3D models going beyond the smooth-flow assumption of our parametrized wind models must be examined before such a possibility can be considered in much greater detail.

7.3 Spectral curvature

Absorption by outflowing material has been discussed as a possible explanation for the so-called soft excess in X-ray spectra (Gierliński & Done 2004, 2006; Middleton, Done & Gierliński 2007; Schurch & Done 2007, 2008). In this picture, the decrease in flux above ~ 1 keV is attributed to absorption by light or intermediate-mass elements.

Such absorption does occur in our models, particularly for high \dot{M} values (see Fig. 12) however the scale of the effect is too small in the models presented here: the typical observed soft excess requires a drop in flux of nearly a factor of two between about 1 and 2 keV (Middleton et al. 2007). Furthermore, Schurch & Done (2008) have argued that very large, relativistic velocities are required for the absorption model to work since the observed soft-excess spectra are very smooth. Our current models support their conclusions since all cases in which significant spectral curvature arises are accompanied by discrete features.

Further consideration must await extension of our calculations to low-ionization states since more significant absorption at relatively soft energies can then be expected.

8 DETAILED COMPARISON WITH Mrk 766

One of the AGN whose X-ray spectrum provided some of the initial motivation for this work is Mrk 766 (Miller et al. 2007; Turner et al. 2007). As well as the possible outflow absorption lines already mentioned in Section 6, Miller et al. (2007) suggested that the extremely hard 2–10 keV spectrum in the low flux state, coupled with the strong Fe edge and weak Fe emission line, might be a signature of either ionized absorption or ionized reflection, possibly from an obscuring wind. Such a picture provides an alternative explanation to the hypothesis of ‘relativistic blurring’ that has been invoked to explain the apparent ‘red wing’ at energies below 7 keV in the mean X-ray spectra of AGN, including Mrk 766 (e.g. Nandra et al. 2007).

We now make a direct comparison between the wind model in this paper and the mean spectrum of Mrk 766 obtained by summing the *XMM-Newton* EPIC pn data from the 2000, 2001 and 2006 observations. Observation IDs were 0096020101, 0096020101 and 0304030[1–7]01 and data were processed as described by Miller et al. (2007). As in that work, energy bins of width equal to the energy-dependent HWHM were adopted. The model was fitted to the data by first creating a multiplicative table (‘mtable’) covering a range of parameters that could be used with *XSPEC* (Arnaud 1996). The models used for this table were those described in Sections 5.1, 5.2 and 5.3 making up a regular, 4D grid covering three of our most important wind parameters (r_{\min} , d and \dot{M}) and the viewing angle (θ). The other wind parameters were not varied in the fit. The table was used to multiply an assumed intrinsic power law whose photon index was a free parameter in the fit: in principle the fitting is valid only for the choice of power-law index used to create the model, but in practice we find that there is little variation between models whose power-law indices differ, and that the variation that is seen is to some extent degenerate with the effects caused by varying other wind parameters (see Section 5). We expect also some amount of spectral curvature caused by the ionized absorption previously identified in Mrk 766, so we add a low column of ionized absorption calculated by *XSTAR* (Kallman et al. 2004) and we model the narrow 6.4 keV Fe emission line as arising in mildly ionized reflection calculated by the *REFLIONX* model (Ross & Fabian 2005) with no relativistic blurring. Owing to computing time limitations the model grid was necessarily rather coarse in parameter space, so to check the fit of the best-fitting model, interpolated between models, we then recalculated the model with precisely the parameter values indicated by fitting. The wind best-fitting parameter were $r_{\min} = 385 r_g$, $d = 1.6 r_{\min}$, $\dot{M} = 0.4 M_{\odot} \text{ yr}^{-1}$ and $\cos \theta = 0.77$, while the best-fitting photon index was $\Gamma = 2.03$ and absorber parameters were $N_H = 5.3 \times 10^{21} \text{ cm}^{-2}$ and ionization parameter $\xi = 40 \text{ erg cm s}^{-1}$. These parameters yielded a goodness of fit $\chi^2 = 145$ for 108 degrees of freedom (no component of systematic error is assumed). The fit to the spectrum in the 2–10 keV range is shown in Fig. 13, where we plot the model spectrum at the *XMM-Newton* resolution together with ‘unfolded’ data points.

The fit of the wind model to the data does indicate that this may well provide a good explanation of the shape of X-ray spectra in AGN such as Mrk 766. With the exception of the narrow Fe emission line, most of the spectral shape in the Fe regime is provided by the wind model, with the reflection component contributing only 3 per cent of the total 2–10 keV energy flux and only 4 per cent of the flux

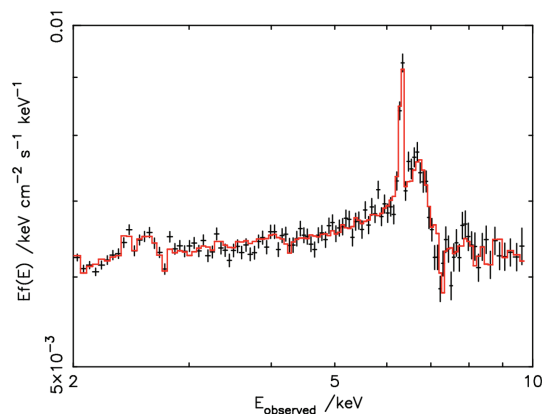


Figure 13. The best-fitting wind model fit to the mean 2–10 keV spectrum of Mrk 766, plotted in units of $E f(E)$, showing model and ‘unfolded’ data.

density in the continuum around Fe. It is unlikely that the current model can explain the full spectral variability seen in this AGN’s various flux states: the hard spectrum in the low state is most likely caused by moderately ionized material, $\xi \simeq 100 \text{ erg cm s}^{-1}$ (Miller et al. 2007), which is not yet treated in the wind model. We postpone to future work fits to the X-ray spectra of this and other AGN with enhanced, lower ionization wind models.

9 CONCLUSIONS AND FUTURE WORK

We have used a simply parametrized model to construct a variety of possible AGN outflow geometries and computed spectra for various lines of sight using a multidimensional MC radiation transport code.

Our results show that narrow blueshifted Fe $K\alpha$ absorption lines are a natural consequence of highly ionized flows and that their formation depends strongly on the flow inclination angles relative to the observer’s line of sight. Typically, our models suggest that moderately strong features $K\alpha$ absorption features ($\gtrsim 40 \text{ eV}$) will manifest for a significant minority of possible viewing angles.

Although blueshifted absorption lines are the clearest signature of an outflow, our calculations have illustrated a number of other spectroscopic signatures which may be relevant to the interpretation of X-ray data in the context of AGN outflows. In particular, electron scattering, line scattering and recombination emission can all affect the Fe K region. For suitable wind conditions and lines of sight, these processes can lead to significant net emission in $K\alpha$ and can make a strong red electron-scattering line wing. We have illustrated that these emission-line profiles look qualitatively similar to observed spectral features (e.g. in Mrk 766) suggesting that outflows may have a much more general role in the formation of AGN X-ray spectra than simply imprinting absorption lines. At the very least, emission/scattering features such as those found in our models must be considered as a potential source of contamination for studies of other sources of Fe K emission.

Considerable further work is required to more fully understand the role of outflows in the spectral formation of AGN. The primary limitation of this study is the restriction to reliable modelling of only K-shell ions. K-shell transitions occurring in lower ions, as may be present in less ionized wind regions, will have a qualitative effect on the Fe K region – e.g. while the $K\alpha$ line of H- and He-like ions predominantly scatter incoming photons, the Li- and Be-like ions can destroy them with significant probability. Fortunately, the restriction to K-shell ions is not a fundamental limitation of the methods used but was made primarily in the interests of

computational expediency for this study of Fe K shell absorption features. The next step will be to extend the physics of the code to incorporate L-shell ions so that lower ionization states may be probed. In particular, this will allow the investigation of outflow geometries with larger r_{max} and flows with a clumpy structure. Furthermore, in this study we have only considered the simplest X-ray source location and have neglected any interplay between different components in the AGN environment. In particular, we have not considered how emission, absorption and reflection by an accretion disc will affect the spectral signatures of outflow, and vice versa. Ultimately, it will be desirable to construct physically motivated models for complete disc/outflow systems and use these to interpret the increasing wealth of X-ray observations.

ACKNOWLEDGMENTS

SAS acknowledges V. Wild for very useful discussions. TJT acknowledges NASA Grant ADP03-0000-00006. We thank the anonymous referee for constructive suggestions.

REFERENCES

- Abbott D. C., Lucy L. B., 1985, *ApJ*, 288, 679
- Arnaud K. A., 1996, in Jacoby G. H., Barnes J., eds, *ASP Conf. Ser. Vol. 101, Astronomical Data Analysis Software and Systems V*. Astron. Soc. Pac., San Francisco, p. 17
- Asplund M., Grevesse N., Sauval A. J., 2005, in Barnes T. G. III, Bash F. N., eds, *ASP Conf. Ser. Vol. 336, Cosmic Abundances as Records of Stellar Evolution and Nucleosynthesis*. Astron. Soc. Pac., San Francisco, p. 25
- Blustin A. J., Page M. J., Fuerst S. V., Branduardi-Raymont G., Ashton C. E., 2005, *A&A*, 431, 111
- Braito V. et al., 2007, *ApJ*, 670, 978
- Croton D. J. et al., 2006, *MNRAS*, 365, 11
- Dere K. P., Landi E., Mason H. E., Monsignori Fossi B. C., Young P. R., 1997, *A&AS*, 125, 149
- Done C., Sobolewska M. A., Gierliński M., Schurch N. J., 2007, *MNRAS*, 374, L15
- Dorodnitsyn A., Kallman T., Proga D., 2008, 801, *ApJ*, 675, L5
- Elvis M., 2000, *ApJ*, 545, 63
- Everett J. E., Ballantyne D. R., 2004, *ApJ*, 615, L13
- Fabian A. C., Rees M. J., Stella L., White N. E., 1989, *MNRAS*, 238, 729
- Fabian A. C., Iwasawa K., Reynolds C. S., Young A. J., 2000, *PASP*, 112, 1145
- Gierliński M., Done C., 2004, *MNRAS*, 349, L7
- Gierliński M., Done C., 2006, *MNRAS*, 371, L16
- Hao C. N., Xia X. Y., Mao S., Wu H., Deng Z. G., 2005, *ApJ*, 625, 78
- Jansen F. et al., 2001, *A&A*, 365, L1
- Kallman T., Bautista M., 2001, *ApJS*, 133, 221
- Kallman T. R., Palmeri P., Bautista M. A., Mendoza C., Krolik J. H., 2004, *ApJS*, 155, 675
- King A. R., Pounds K. A., 2003, *MNRAS*, 345, 657
- Knigge C., Woods J. A., Drew J. E., 1995, *MNRAS*, 273, 225
- Laming J. M., Titarchuk L., 2004, *ApJ*, 615, L121
- Landi E., Del Zanna G., Young P. R., Dere K. P., Mason H. E., Landini M., 2006, *ApJS*, 162, 261
- Laurent P., Titarchuk L., 2007, *ApJ*, 656, 1056
- Long K. S., Knigge C., 2002, *ApJ*, 579, 725
- Lucy L. B., 1999, *A&A*, 345, 211
- Lucy L. B., 2002, *A&A*, 384, 725
- Lucy L. B., 2003, *A&A*, 403, 261
- Lucy L. B., 2005, *A&A*, 429, 19
- Lucy L. B., Abbott D. C., 1993, *ApJ*, 405, 738
- Martin P. G., 1988, *ApJS*, 66, 125
- Mazzali P. A., Lucy L. B., 1993, *A&A*, 279, 447
- McKernan B., Yaqoob T., Reynolds C. S., 2007, *MNRAS*, 379, 1359
- Middleton M., Done C., Gierliński M., 2007, *MNRAS*, 381, 1426
- Miller J. M., 2007, *ARA&A*, 45, 441
- Miller L., Turner T. J., Reeves J. N., George I. M., Kraemer S. B., Wingert B., 2007, *A&A*, 463, 131
- Miller L., Turner T. J., Reeves J. N., 2008, *A&A*, 483, 437
- Miniutti G. et al., 2007, *PASJ*, 59, 315
- Mitsuda K. et al., 2007, *PASJ*, 59, 1
- Murray N., Chiang J., Grossman S. A., Voit G. M., 1995, *ApJ*, 451, 498
- Nandra K., George I. M., Mushotzky R. F., Turner T. J., Yaqoob T., 1997, *ApJ*, 477, 602
- Nandra K., O'Neill P. M., George I. M., Reeves J. N., 2007, *MNRAS*, 382, 194
- O'Neill P. M., Nandra K., Cappi M., Longinotti A. L., Sim S. A., 2007, *MNRAS*, 381, L94
- Pounds K. A., Page K. L., 2006, *MNRAS*, 372, 1275
- Pounds K. A., Reeves J. N., 2007, *MNRAS*, 374, 823
- Pounds K. A., Reeves J. N., King A. R., Page K. L., O'Brien P. T., Turner M. J. L., 2003a, *MNRAS*, 345, 705
- Pounds K. A., Reeves J. N., Page K. L., Wynn G. A., O'Brien P. T., 2003b, *MNRAS*, 342, 1147
- Pounds K. A., Reeves J. N., King A. R., Page K. L., O'Brien P. T., Turner M. J. L., 2005, *MNRAS*, 356, 1599
- Proga D., Kallman T. R., 2004, *ApJ*, 616, 688
- Reeves J. N., Nandra K., George I. M., Pounds K. A., Turner T. J., Yaqoob T., 2004, *ApJ*, 602, 648
- Risaliti G., Bianchi S., Matt G., Baldi A., Elvis M., Fabbiano G., Zezas A., 2005, *ApJ*, 630, L129
- Ross R. R., Fabian A. C., 2005, *MNRAS*, 358, 211
- Róźańska A., Madej J., 2008, *MNRAS*, 386, 1872
- Schurch N. J., Done C., 2007, *MNRAS*, 381, 1413
- Schurch N. J., Done C., 2008, 709, *MNRAS*, 386, L1
- Shapiro S. L., Teukolsky S. A., 1983, *Black Holes, White Dwarfs, and Neutron Stars: The Physics of Compact Objects*. Wiley-Interscience, New York, p. 663
- Sim S. A., 2005, *MNRAS*, 356, 531
- Sim S. A., Drew J. E., Long K. S., 2005, *MNRAS*, 363, 615
- Turner T. J., Miller L., Reeves J. N., Kraemer S. B., 2007, *A&A*, 475, 121
- Turner T. J., Reeves J. N., Kraemer S. B., Miller L., 2008, *A&A*, 483, 161
- Verner D. A., Ferland G. J., Korista K. T., Yakovlev D. G., 1996, *ApJ*, 465, 487
- Verner D. A., Yakovlev D. G., 1995, *A&AS*, 109, 125
- Vink J. S., de Koter A., Lamers H. J. G. L. M., 1999, *A&A*, 350, 181
- Wang T., Lu Y., 2001, *A&A*, 377, 52
- Weisskopf M. C., Brinkman B., Canizares C., Garmire G., Murray S., Van Speybroeck L. P., 2002, *PASP*, 114, 1
- Young A. J., Lee J. C., Fabian A. C., Reynolds C. S., Gibson R. R., Canizares C. R., 2005, *ApJ*, 631, 733

This paper has been typeset from a \LaTeX file prepared by the author.